

Unsupervised CT Metal Artifact Reduction by Plugging Diffusion Priors in Dual Domains

Xuan Liu, Yaoqin Xie, Songhui Diao, Shan Tan, *Member, IEEE*, and Xiaokun Liang, *Member, IEEE*

Abstract—During the process of computed tomography (CT), metallic implants present within patients often lead to disruptive artifacts in reconstructed images, which can hinder accurate diagnosis. Many supervised deep learning-based approaches have been proposed for metal artifact reduction (MAR). However, these methods rely on extensive training with simulated data, as acquiring paired metal artifact CT and clean CT data in clinical settings is challenging. This limitation can result in diminished performance when applying them in clinical practice. Existing effective unsupervised MAR methods, whether based on learning or not, often work with single-domain processing, either in the image domain or the sinogram domain. In this paper, we introduce an unsupervised MAR method based on diffusion model, a generative model with a potent capacity to represent data distributions. Concretely, we first train a diffusion model with CT images without metal artifacts. Subsequently, we iteratively utilize the priors embedded within the pre-trained diffusion model in both the sinogram domain and the image domain, aiming to restore the degraded portions caused by metal artifacts. The dual domain processing empowers our approach to outperform existing unsupervised MAR methods, including another MAR method based on diffusion model, which has been qualitatively and quantitatively validated on synthetic datasets. Additionally, our method demonstrates superior visual results among both supervised and unsupervised methods on clinical datasets. Codes are available in github.com/DeepXuan/DuDoDp-MAR.

Index Terms—Computed tomography, Metal artifact reduction, Diffusion model, Unsupervised learning

I. INTRODUCTION

COMPUTED tomography plays a crucial role in modern medicine for diagnosis and treatment. However, metallic

implants within patients will cause severe artifacts in reconstructed CT images [1], [2], which can significantly impact subsequent diagnostic procedures. The presence of metallic implants will make part of the sinogram values abnormal. CT image reconstructed from such abnormal sinogram always exhibit disruptive artifacts in non-metal regions [3]. Therefore, numerous algorithms have been designed to alleviate metal artifacts in reconstructed CT images when the sinogram is contaminated by metal.

The most commonly employed traditional methods for metal artifact reduction (MAR) are based on sinogram inpainting, which remove and inpaint the metal-affected regions in the sinogram before performing the reconstruction process. Kalender et al. proposed to fill the hollow sinogram using linear interpolation (LI) [3]. Meyer et al. proposed normalized metal artifact reduction (NMAR) to replace the metal-affected regions in sinogram with the forward projection of a prior image [4]. Although LI and NMAR are both simple and effective MAR methods, the reconstructed images may still contain artifacts due to the potential discontinuities at the edges of the completed sinogram.

With the rapid development of deep learning techniques over the past decade, numerous MAR methods based on deep learning have been proposed, exhibiting significant improvements compared to traditional methods. The majority of deep learning-based MAR methods are supervised, relying on paired metal artifact CT and clean CT data to train neural networks [5]–[9]. The same as traditional methods, deep learning-based MAR methods can work in sinogram domain, image domain, or both. Park et al. proposed to use a convolutional neural network (CNN) to repair inconsistent sinogram caused by beam hardening [2]. Zhang et al. proposed CNNMAR that produce a prior image by a CNN then complete the metal-affected sinogram with the forward projection of the prior image [10]. Besides, post-processing deep neural networks attempt to directly learn the mapping from metal artifact CT images to clean CT images. Huang et al. conducted MAR for cervical CT images with deep residual learning [11]. Wang et al. used generative adversarial networks (GAN) [12] for MAR of ear CT images [13]. By utilizing information from both the sinogram domain and the image domain, some dual-domain networks have been proposed to simultaneously restore sinogram consistency and enhance CT images. Lin et al. proposed an end-to-end trainable dual domain Network (DuDoNet) [5]. Zhou et al. proposed a dual-domain data consistent recurrent network (DuDoRNet) [8]. Wang et al. pro-

This work is partly supported by grants from the National Natural Science Foundation of China (62071197, 82202954, U20A20373, U21A20480, 12126608) and the Chinese Academy of Sciences Special Research Assistant Grant Program. (Corresponding author: Shan Tan and Xiaokun Liang.)

Xuan Liu is with the School of Artificial Intelligence and Automation, Huazhong University of Science and Technology, Wuhan 430074, China and the Institute of Biomedical and Health Engineering, Shenzhen Institutes of Advanced Technology, Chinese Academy of Sciences, Shenzhen 518055, China (e-mail: liuxuan99@hust.edu.cn).

Shan Tan is with the School of Artificial Intelligence and Automation, Huazhong University of Science and Technology, Wuhan 430074, China (e-mail: shantan@hust.edu.cn).

Yaoqin Xie, Songhui Diao, and Xiaokun Liang are with the Institute of Biomedical and Health Engineering, Shenzhen Institutes of Advanced Technology, Chinese Academy of Sciences, Shenzhen 518055, China (e-mail: yq.xie@siat.ac.cn, sh.diao@siat.ac.cn, xk.liang@siat.ac.cn).

posed an interpretable dual domain network (InDuDoNet) [6] and its improved version, InDuDoNet+ [9]. The dual domain networks process both of the sinogram data and image data successively or recurrently and achieve better performance compared with single domain networks.

However, training an MAR neural network in a supervised manner requires large amounts of paired CT data with and without metal artifacts, which are practically unattainable in clinical. As a result, supervised methods often have to be trained exclusively on simulated data, which can lead to suboptimal results in clinical applications due to domain gaps. Consequently, some unsupervised or weakly supervised methods have been proposed to address the issue of lacking paired training data. Liao et al. introduced the first unsupervised learning approach to MAR named artifact disentanglement network (ADN), which realized translation between metal-affected image and clean image [14]. Du et al. proposed a novel MAR method based on unsupervised domain adaptation (UDA) called UDAMAR to tackle the domain gap problem [15]. In addition, certain general unsupervised image-to-image translation methods can also be employed for MAR, such as CycleGAN [16], MUNIT [17]. These prevalent unsupervised MAR methods work within the image domain. However, due to the severe and unstructured nature of metal artifacts in the image domain, the effectiveness of these methods, particularly in terms of visual quality, is often limited. Song et al. proposed a novel approach for MAR, wherein they formulated the task as a linear inverse problem and utilized a pre-trained score model [18] as a regularizer [19]. Specifically, they iteratively performed inpainting on the hollow regions in the sinogram domain using prior images from the score model. The method is insightful but we consider it doesn't fully leverage the powerful capabilities of score models because the combination of the priors provided by the score model and the known portions only occurs in the sinogram domain.

In order to address the limitations of existing unsupervised MAR methods, we proposed a novel method for MAR that utilize the priors embedded within a pre-trained diffusion model [20] in both sinogram domain and image domain. Concretely, we first train a diffusion model with large amounts of CT images without metal artifacts for preparation. The well-trained is not only capable of generating visually realistic clean CT images but can also represent its distribution using analytical probability density functions. Subsequently, we extract the metal-affected portions from the sinogram and model MAR as a reconstruction problem with partial measurement missing. This problem is solved iteratively. At each timestep of the diffusion generation process, we first fuse the output of diffusion and the known sinogram in the sinogram domain. Due to the discontinuity between the prior sinogram provided by the diffusion model and the known sinogram, the reconstructed image might introduce new artifacts in the image domain. Therefore, we reintroduce the diffusion priors in the image domain to mitigate this issue. Besides, to ensure a balance between likelihood and prior, we meticulously design weight masks for the fusion in the image domain and validate their effectiveness.

We name this **dual domain** method with **diffusion** priors as

DuDoDp. Our contributions can be summarized as follows:

- 1) We present a MAR method that combines diffusion priors within a dual domain framework to fully leverage the information from both the sinogram domain and the image domain.
- 2) We propose to fuse three kinds of images at each timestep, which are prior images from diffusion model, reconstructed images from inpainted sinogram, and original metal-artifact images. The combination of these images corrects the artifacts caused by sole sinogram inpainting.
- 3) We design dynamic weight masks to control the addition of diffusion priors. According to the iterative generation nature of diffusion, we dynamically adjust the masks over timesteps to achieve enhanced results.
- 4) The proposed method is validated in both synthetic and clinical datasets, demonstrating its potential for clinical applications.

II. METHOD

A. Preliminary

1) *Diffusion Model*: The diffusion model (short for denoising diffusion probabilistic model) is a kind of deep generative model [18], [20]. Given a set of data $x_0 \sim q(x_0)$, a diffusion model defines a fixed forward process that gradually add Gaussian noise to the original data. Then it attempts to learn a reverse process to reverse the forward process and realize image generation from random noise. Generally, the forward process $q(x_{1:T} | x_0)$ is defined as a Markov chain, which means the status at each timestep is only related on the previous timestep. Specifically, there is:

$$q(x_{1:T} | x_0) := \prod_{t=1}^T q(x_t | x_{t-1}), q(x_t | x_{t-1}) := \mathcal{N}(x_t; \sqrt{1 - \beta_t}x_{t-1}, \beta_t I), \quad (1)$$

where x_t is the data at timestep t , $\mathcal{N}(\cdot; \mu, \Sigma)$ denotes a Gaussian distribution with mean μ and covariance matrix Σ , and $\{\beta_1, \dots, \beta_T\}$ is a fixed variance schedule. Based on (1), the following two conditional distributions are derived:

$$q(x_t | x_0) = \mathcal{N}(x_t; \sqrt{\bar{\alpha}_t}x_0, (1 - \bar{\alpha}_t)I), \quad (2)$$

$$q(x_{t-1} | x_t, x_0) = \mathcal{N}(x_{t-1}; \tilde{\mu}_t(x_t, x_0), \tilde{\beta}_t I), \quad (3)$$

where,

$$\bar{\alpha}_t := \prod_{i=1}^t (1 - \beta_i), \quad (4)$$

$$\tilde{\mu}_t(x_t, x_0) := \frac{\sqrt{\bar{\alpha}_{t-1}}\beta_t}{1 - \bar{\alpha}_t}x_0 + \frac{\sqrt{\alpha_t}(1 - \bar{\alpha}_{t-1})}{1 - \bar{\alpha}_t}x_t, \quad (5)$$

$$\tilde{\beta}_t := \frac{(1 - \bar{\alpha}_{t-1})}{1 - \bar{\alpha}_t}\beta_t. \quad (6)$$

Then we define the reverse process as a Markov chain with learnable parameters θ ,

$$p_\theta(x_{0:T}) := p(x_T) \prod_{t=1}^T p_\theta(x_{t-1} | x_t), \quad (7)$$

where,

$$p(x_T) = \mathcal{N}(x_T; 0, I), \quad (8)$$

$$p_\theta(x_{t-1} | x_t) := \mathcal{N}(x_{t-1}; \mu_\theta(x_t, t), \sigma_t^2 I). \quad (9)$$

Here, $\mu_\theta(x_t, t)$ is predicted by trainable neural networks, and σ_t^2 is defined as $\frac{1-\bar{\alpha}_t}{1-\bar{\alpha}_t} \beta_t$. The training loss is derived by minimizing the variational bound of the negative log likelihood $-\log p_\theta(x_0)$ [20].

2) ϵ -Prediction and x_0 -Prediction Diffusion Model: Generally, a diffusion model doesn't directly predict the mean values $\mu_\theta(x_t, t)$ in (9) at each timestep. Alternatively, it's more common to predict the added noise ϵ_t or the initial image x_0 from x_t , where $x_t = \sqrt{\bar{\alpha}_t}x_0 + \sqrt{1-\bar{\alpha}_t}\epsilon_t$. The relationship between the predicted noise $\epsilon_\theta(x_t, t)$ and $\mu_\theta(x_t, t)$ is [20],

$$\begin{aligned} \mu_\theta(x_t, t) &= \tilde{\mu}_t \left(x_t, \frac{1}{\sqrt{\bar{\alpha}_t}} (x_t - \sqrt{1-\bar{\alpha}_t}\epsilon_\theta(x_t, t)) \right) \\ &= \frac{1}{\sqrt{\bar{\alpha}_t}} \left(x_t - \frac{\beta_t}{\sqrt{1-\bar{\alpha}_t}} \epsilon_\theta(x_t, t) \right), \end{aligned} \quad (10)$$

where $\tilde{\mu}_t$ is from (5). Predicting $\epsilon_\theta(x_t, t)$ from x_t makes the training of diffusion models more concise to implement, which equals predicting the added noise ϵ_t from the noisy image x_t and noise level t [20].

Naturally, we can also predict the latent clean images x_0 from x_t . Let the prediction of x_0 be $f_\theta(x_t, t)$, we have,

$$f_\theta(x_t, t) = (x_t - \sqrt{1-\bar{\alpha}_t}\epsilon_\theta(x_t, t))/\sqrt{\bar{\alpha}_t}. \quad (11)$$

Under this setting, the inference process of the diffusion model in (9) can be rewritten as follows [21],

$$p_\theta(x_{t-1} | x_t) = q(x_{t-1} | x_t, f_\theta(x_t, t)), \quad (12)$$

where $q(x_{t-1} | x_t, f_\theta(x_t, t))$ is calculated according to (3).

Regardless of whether predicting μ_θ , ϵ_θ , or f_θ , the principles of a diffusion model and the meaning of its training loss remain unchanged. The only difference lies in the interpretation of the neural network outputs.

B. MAR with Dual Domain Diffusion Priors

In this section, we introduce DuDoDp, a MAR method with dual-domain diffusion priors. Firstly, in Section II-B.1, we introduce the diffusion priors into the MAR problem by iteratively solving multiple optimization problems. This incorporation is equivalent to employing the prior image provided by diffusion model for inpainting in the sinogram domain. To alleviate the artifacts arising from the discontinuities in the inpainted sinogram, we propose further integration of the diffusion prior in the image domain, as outlined in Section II-B.2. In Section II-B.3, we design weight masks for image domain fusion, and considering the iterative nature of diffusion, dynamic masks are employed at different timesteps. The overall algorithm workflow is illustrated in Fig. 1.

1) Introduction of Diffusion Priors for MAR: The MAR problem can be viewed as the task of reconstructing a clean images x_0 from sinogram s_0 affected by metal. Directly applying analytical algorithms such as filtered back-projection (FBP) for reconstruction will result in an image y_0 with metal artifacts, where $y = \text{FBP}(s_0)$. Typically, we are aware of which parts of the sinogram are affected by metal, represented by a boolean mask \mathcal{M}_s . In this mask, the unaffected portions are denoted as 0, while the affected parts are marked as 1. The relationship between s_0 and x_0 is,

$$(1 - \mathcal{M}_s) \odot s_0 = (1 - \mathcal{M}_s) \odot \text{FP}(x_0) \quad (13)$$

Therefore, the MAR problem can be formulated as,

$$\min_{x_0} \|(1 - \mathcal{M}_s) \odot (\text{FP}(x_0) - s_0)\|^2 + \lambda \mathcal{R}(x_0), \quad (14)$$

where $\text{FP}(\cdot)$ denotes the forward projection function of the CT system, \odot denotes the Hadamard product, $\mathcal{R}(\cdot)$ denotes a regularizer for the clean image x_0 , and λ is a coefficient.

We attempt to get the regularizer \mathcal{R} from a pre-trained diffusion model. However, a diffusion model doesn't directly represent the probability density function of the data but obtains it iteratively. Specifically, with known x_t , the probability density function of the data at timestep $t-1$ is $q(x_{t-1} | x_t, f_\theta(x_t, t))$ according to (12).

To utilize the prior at timestep $t-1$, we can iteratively solve x_{t-1} that has a clear relationship with x_0 according to (3),

$$x_{t-1} = \tilde{\mu}_t(x_t, x_0) + \sqrt{\beta_t} z_{t-1}, \quad (15)$$

where $\tilde{\mu}_t$ is from (5) and $z_{t-1} \sim \mathcal{N}(0, I)$. Similarly, we can define a way to get s_{t-1} ,

$$s_{t-1} = \tilde{\mu}_{t-1}(\text{FP}(x_t), s_0) + \text{FP}(\sqrt{\tilde{\beta}_t} z_{t-1}). \quad (16)$$

In this way, we have,

$$(1 - \mathcal{M}_s) \odot s_{t-1} = (1 - \mathcal{M}_s) \odot \text{FP}(x_{t-1}) \quad (17)$$

According to (17), at each time step $t-1$, we can iteratively solve such an optimization problem,

$$\begin{aligned} \min_{x_{t-1}} &\|(1 - \mathcal{M}_s) \odot (\text{FP}(x_{t-1}) - s_{t-1})\|^2 \\ &+ \lambda q(x_{t-1} | x_t, f_\theta(x_t, t)). \end{aligned} \quad (18)$$

With (18), we have successfully incorporated the priors provided by the diffusion model into the solution of the MAR problem through an iterative approach. Because both x_{t-1} and s_{t-1} are transformed from x_0 and s_0 in the same way (see (15) and (16)), by eliminating certain coefficients, (18) becomes,

$$\begin{aligned} \min_{\tilde{x}_0^{t-1}} &\|(1 - \mathcal{M}_s) \odot (\text{FP}(\tilde{x}_0^{t-1}) - s_0)\|^2 \\ &+ \lambda' \|\tilde{x}_0^{t-1} - f_\theta(x_t, t)\|^2, \end{aligned} \quad (19)$$

Where \tilde{x}_0^{t-1} denotes the predicted initial image at timestep $t-1$, λ' is a coefficient that won't be used for solving (19). As for the convex optimization problem in (19), numerous iterative algorithms are available for solving this. However, to mitigate the issue of prolonged computational time associated with iterative solving, we directly use the forward projection

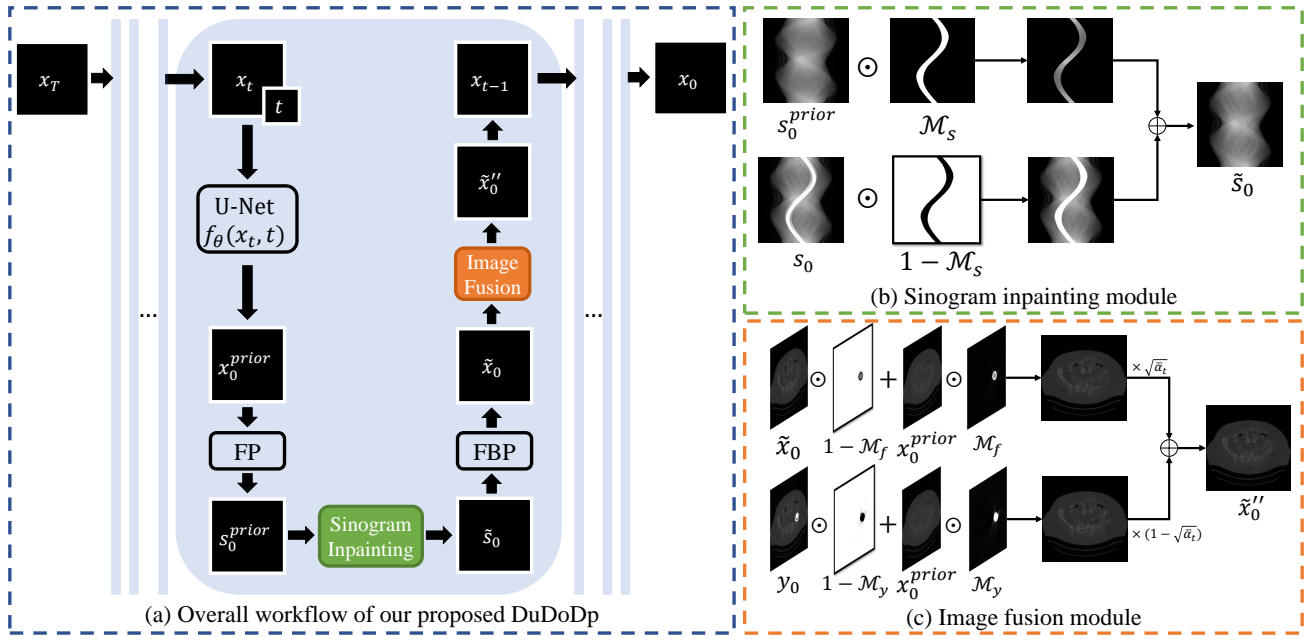


Fig. 1. (a) illustrates the overall workflow of our MAR method, DuDoDp. Each blue box shows one iteration to calculate x_{t-1} from x_t . (b) and (c) respectively illustrate the sinogram inpainting module and image fusion module in (a).

of $f_\theta(x_t, t)$ to inpaint the metal-affected sinogram and derive the inpainted result \tilde{s}_0^{t-1} , which satisfies,

$$\tilde{s}_0^{t-1} = \begin{cases} s_0, & \text{where } \mathcal{M}_s = 0, \\ s_0^{prior}, & \text{where } \mathcal{M}_s = 1, \end{cases} \quad (20)$$

where $s_0^{prior} = \text{FP}(f_\theta(x_t, t))$. Then, \tilde{x}_0^{t-1} can be approximately reconstructed by FBP from \tilde{s}_0^{t-1} ,

$$\tilde{x}_0^{t-1} = \text{FBP}(\tilde{s}_0^{t-1}). \quad (21)$$

\tilde{x}_0^{t-1} can be regarded as an approximation to (19). Then, x_{t-1} can be derived from \tilde{x}_0^{t-1} according to the posterior distribution of (3)¹.

Through the above-mentioned approach, we have integrated the diffusion priors into the MAR framework, corresponding to the sinogram inpainting component in Fig. 1(b).

2) Fusion Strategy in Image Domain: Although solving (19) using the methods outlined in (20) and (21) is efficient, the prior sinogram $\mathcal{M}_s \odot \text{FP}(f_\theta(x_t, t))$ provided by the diffusion model exhibits discontinuities with the known sinogram $(1 - \mathcal{M}_s) \odot s_0$. This leads to the introduction of new artifacts when using FBP reconstruction, as depicted in Fig. 2.

Therefore, we propose further refining the reconstructed image \tilde{x}_0^{t-1} using the diffusion prior in the image domain. Firstly, we add the diffusion-predicted x_0 at timestep $t-1$, as well as $f_\theta(x_t, t)$, to \tilde{x}_0^{t-1} with a certain weight mask,

$$\tilde{x}_0'^{t-1} = \mathcal{M}_f \odot f_\theta(x_t, t) + (1 - \mathcal{M}_f) \odot \tilde{x}_0^{t-1}, \quad (22)$$

where \mathcal{M}_f denotes the weight mask for diffusion prior $f_\theta(x_t, t)$, which help correct the unnatural portions of \tilde{x}_0^{t-1} .

¹In practical experiments, we achieve better results by using conditional probability sampling as outlined in (2) to obtain x_{t-1} , which doesn't involve x_t again.

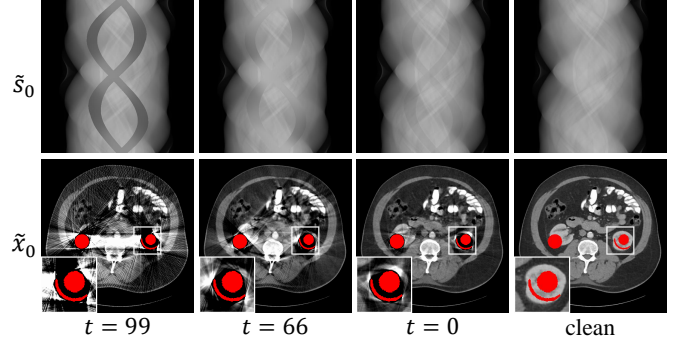


Fig. 2. The intermediate results (T=100) using the diffusion priors only in the sinogram domain is shown. The red parts indicate metallic implants. It can be observed that, in the early iterations, the discontinuities of inpainted sinogram lead to artifacts beyond the metal regions, and part of these artifacts persists even after the completion of iterations. The display window of CT images is [-175, 275] HU.

In addition, we propose further fusing the original metal-artifact image y_0 into \tilde{x}_0' . This can provide additional likelihood information. The specific approach involves,

$$\tilde{y}_0 = \mathcal{M}_y \odot f_\theta(x_t, t) + (1 - \mathcal{M}_y) \odot y_0, \quad (23)$$

$$\tilde{x}_0''^{t-1} = \sqrt{\alpha_t} \tilde{x}_0'^{t-1} + (1 - \sqrt{\alpha_t}) \tilde{y}_0. \quad (24)$$

Eq. (23) demonstrates the fusion of the metal-artifact image with the prior image using a certain weight mask \mathcal{M}_y . Eq. (24) illustrates the combination of the metal-artifact image that has been merged with the prior (as in (23)) and the prior-enhanced reconstructed image (from (22)) using a specific ratio. The coefficients are derived from the hyper-parameters of the diffusion forward process. This indicates that as t decreases, the proportion of the metal-artifact image becomes smaller.

The algorithm for the image-domain fusion described above

is depicted in Fig. 1(c). In Section IV.A, We verify the performance enhancement brought by introducing image-domain fusion strategies to MAR.

3) *Temporally Dynamic Weight Masks*: Selecting proper \mathcal{M}_f and \mathcal{M}_y is challenging. Empirically, we propose to construct the weight mask utilizing the reconstructed results from binary sinogram as,

$$\mathcal{M}(\delta) = \text{FBP}(\delta \mathcal{M}_s), \quad (25)$$

where δ means the value filled in the metal-affected regions while other regions are filled with zeros. Generally, as δ increases, the overall values of the reconstructed weight mask also increase, as illustrated in Fig. 3².

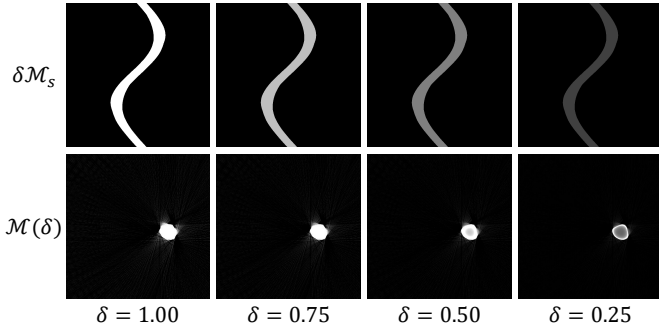


Fig. 3. Binary sinogram corresponding to different δ values and their reconstructed weight masks. With smaller δ values, the resulting weight masks are generally smaller (darker in the images).

For \mathcal{M}_y , using a fixed δ is reasonable since in (23) y_0 remains unchanged. Therefore, we set it as,

$$\mathcal{M}_y = \mathcal{M}(\delta_y). \quad (26)$$

However, for \mathcal{M}_f , at different timesteps, differences between the known sinogram $(1 - \mathcal{M}_s) \odot s_0$, and prior sinogram $\mathcal{M}_s \odot \text{FP}(f_\theta(x_t, t))$ will cause the variations in image domain artifacts. Generally, as the value of timestep t decreases, the generation of diffusion model becomes more realistic, resulting in reduced discontinuities in inpainted sinogram and subsequently minimizing artifacts in the image domain. Therefore, designing a weight mask that varies with the timestep t is more reasonable,

$$\mathcal{M}_f(t) = \mathcal{M}(\delta(t)), \quad (27)$$

where $\delta(t)$ is a value varying with t . Then, replace \mathcal{M}_f in (22) with $\mathcal{M}_f(t)$ to achieve a more accurate fusion result. In Section IV-A.2, we validate the positive impact of the temporally dynamic \mathcal{M}_f on the MAR results.

III. IMPLEMENTATION DETAILS

A. Datasets

1) *Training Dataset*: To train our diffusion model, we use the CT images without metal-artifacts from the DeepLesion dataset [22]. Excluding the 200 CT images reserved for testing, there are a total of 927,802 512×512 CT images used for training.

²Before reconstruction, the values of the sinogram are multiplied by 4.0, which corresponds to the maximum sinogram value in our experiments.

2) *Synthetic Test Dataset*: We firstly evaluate our proposed methods as well as the comparison methods on a synthetic dataset, where 200 clean CT images from DeepLesion dataset are chosen to simulate metal-artifact CT images. 10 metal masks are individually implanted into each CT image, followed by using fan-beam projection simulation to obtain the metal-affected sinogram. In total, 2000 sets of CT sinogram and images affected by metal artifacts are obtained for evaluating the MAR methods. The masks are from CNRMAR [10] and the sizes of the 10 metal masks are [2061, 890, 881, 451, 254, 124, 118, 112, 53, 35] in pixels. The fan-beam geometry follows a previous work of Yu et al [23]. During the fan-beam projection process, the CT images were first resized to 416×416 . Then, a total of 640 projections were evenly taken within the angle range of 0 to 2π . The detector has 641 bins, resulting in a projection size of 640×641 . During the simulation of metal artifacts, several effects are taken into consideration, including polychromatic X-ray, partial volume effect, beam hardening, and Poisson noise. This synthetic dataset is widely used in previous works [5]–[9], [14].

3) *clinical Test Dataset*: We further conduct test of our method on the CTPelvis1k dataset [24]. The sub-dataset clinical-metal of CTPelvis1k contains postoperative CT images with metal artifacts. The clinical CT images are firstly resized to 416×416 . Then, following the same projection principle with synthetic DeepLesion data, we acquire the sinogram of the clinical data. We segment the metallic implants using a threshold of 2500 HU and obtain the metal trace in the sinogram through forward projection.

B. Network Architecture and Diffusion Parameters

We choose patch diffusion [25] for our pre-training, which is an improved version of guided diffusion [26]. Patch diffusion proposes to first reshape the image into a grid of non-overlapping patches and concatenate them in channel dimension, then learn the generation of the reshaped images. This approach reduces the compute requirements for generating high-resolution images. In our experiments, we divide the $512 \times 512 \times 1$ images into patches of shape $128 \times 128 \times 16$.

In the training of diffusion, we opt for the method of predicting x_0 , where in each iteration, the network outputs $f_\theta(x_t, t)$ to predict the initial image, as (11). In terms of network architecture, we employ the U-net architecture from guided diffusion. Some of the network parameters are listed in Table 1, where Dim denotes the number of initial channel dimensions, Muls ($\{m[1], \dots, m[k]\}$) denotes the channel multipliers, N-Res denotes the number of residual blocks, Res-Attn denotes the resolution at which a self-attention residual block is employed, Dropout denotes the dropout rate, and Ch-Head denotes the number of channels per head.

TABLE I
DETAILED PARAMETERS OF THE U-NETS ARCHITECTURE.

Dim	Muls	N-Res	Res-Attn	Dropout	Ch-Head
d	$\{m[1], \dots, m[k]\}$				
128	$\{1, 1, 2, 2, 4\}$	2	16, 8	0.0	64

We set the batch size to 16, learning rate to 1.0×10^{-4} , and train the model for 150,000 iterations. The training is conducted on a single RTX 3090 GPU.

During the sampling phase, we employ an acceleration technique to reduce the number of timesteps for improved sampling efficiency [26]. Specifically, we uniformly downsample the hyper-parameters $\{\beta_1, \dots, \beta_T\}$ of the forward process, reducing their count from 1000 to 100. Subsequently, we use the new hyper-parameter schedule in the inference of diffusion to achieve acceleration.

C. Evaluation Metrics

For the simulation dataset, where ground truth is available, we employ peak signal-to-noise ratio (PSNR) and structural similarity index (SSIM) as evaluation metrics. We divide the test images into five groups based on the sizes of the implanted metal masks, from large to small, and calculate average metrics for each group. The grouping is [(2061), (890, 881), (451, 254), (124, 118, 112), (53, 35)]. The metrics are calculated with the HU window [-1000, 4208]. Simultaneously, we showcase the visual effects of different methods in terms of metal artifact reduction for various sizes of metallic implants.

In the case of real clinical datasets, the absence of ground truth restricts us to using visual assessment as the criterion for evaluating algorithm performance.

IV. EXPERIMENTS

A. Ablation Study

In this subsection, we validate the effectiveness of different modules proposed in Section II-B, including sinogram inpainting and image fusion. The image fusion module encompasses whether to introduce an initial metal-artifact (MA) image. Furthermore, we explore how to select dynamic weight masks to further enhance algorithm performance.

1) *Validation of Modules:* We validate the MAR performance of using sinogram inpainting or image fusion strategies separately and using them simultaneously on the synthetic DeepLesion dataset³. We divide image domain fusion into two parts for validation: one represented by (22), fusing the prior image from diffusion model (denoted as '+Prior Image' in Table II; and the other represented by (23) and (24), involving fusion with the initial metal artifact image (denoted as '+MA Image' in Table II. Table II presents the quantitative metrics.

TABLE II
METRICS OF USING DIFFERENT MODULES IN DuDoDP

Label	Sino Domain	Image Domain		PSNR	SSIM
	Sino Inpainting	+Prior Image	+MA Image		
(a)	✓	✗	✗	43.04	0.988
(b)	✗	✗	✓	40.14	0.951
(c)	✓	✓	✗	43.65	0.988
(d)	✓	✓	✓	43.80	0.989

³Here, we utilized constant \mathcal{M}_f and \mathcal{M}_y , where $\mathcal{M}_f = \mathcal{M}(1.0)$, $\mathcal{M}_y = \mathcal{M}(0.8)$.

From Table II, it can be observed that starting with sinogram inpainting as the foundation achieves an initial reduction of metal artifacts. Image domain fusion further enhances the effectiveness, particularly evident in the improved PSNR. It's evident that each module we proposed has a positive impact.

It's worth noting that we test the effect of solely using the metal artifact image for image domain fusion without sinogram inpainting, as in experiment (b) in Table II. The process involved iterating according to (23) without the fusion from (24). The results indicate poorer performance, which can be attributed to the complexity of metal artifacts in the image domain. This demonstrates the necessity of dual-domain processing. From Fig. 4, we can observe that neither

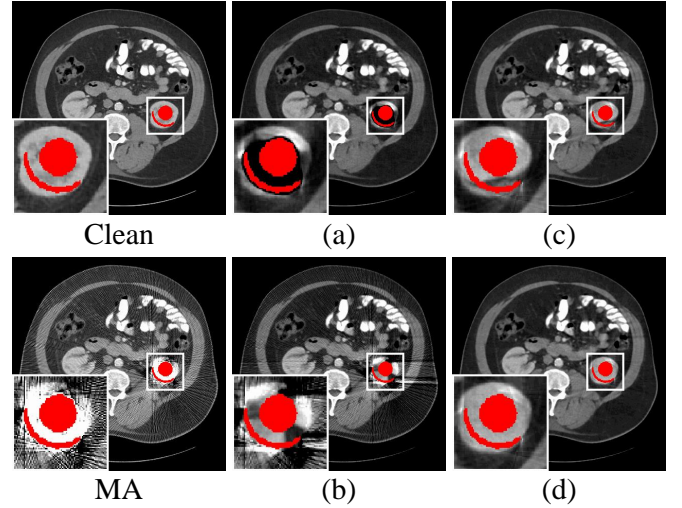


Fig. 4. The visual effects of our MAR methods using different modules, where the red parts indicate metallic implants. (a-d) correspond to the experimental setups in Table II. The display window is [-175, 275] HU.

using only sinogram domain processing nor image domain processing could successfully recover the image around the metallic implant. However, incorporating image domain fusion after sinogram inpainting leads to improved recovery around the metallic region. The best visual results are achieved when fusing both the diffusion prior image and the original metal artifact image.

2) *Validation of Dynamic Weight Masks:* In section II-B.3, we introduce the use of temporally dynamic weight masks \mathcal{M}_f to fuse the diffusion prior image and the reconstructed image from inpainted sinogram. Here, we test how to choose the time-varying $\delta(t)$ to generate the dynamic masks $\mathcal{M}_f(t) = \mathcal{M}(\delta(t))$. Empirically, as the value of timestep t decreases, the artifacts in the image domain become slighter. Hence, we set $\delta(t)$ as a function that positively correlates with timestep t ,

$$\delta(t) = (a - 1)e^{-n \frac{t}{T}} + 1. \quad (28)$$

With this design, for a large n value, $\delta(t)$ approaches 1 at $t = T$, while at $t = 0$, $\delta(t) = a$. Choosing different values of a and n yields different functions, as illustrated in Fig. 5, where we select $a = (0.3, 0.4, 0.5)$ and $n = (3, 4, 5)$ and plot the nine $\delta(t)$ functions obtain from these combinations.

We test the dynamic masks corresponding to the nine $\delta(t)$ functions from Fig. 5 on the synthetic DeepLesion dataset.

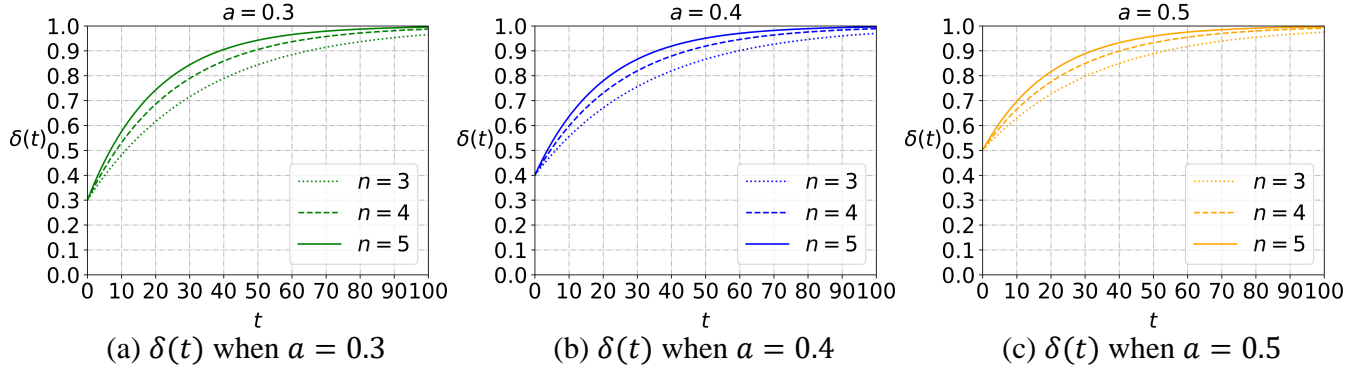


Fig. 5. Functions of $\delta(t)$ when $a = 0.3, 0.4, 0.5$ and $n = 3, 4, 5$.

Table III presents the corresponding PSNR values, where $a = 1.0$ mean a constant weight mask because $\delta(t) = 1$.

TABLE III

PSNRs OF USING DIFFERENT DYNAMIC WEIGHT MASKS OR USING CONSTANT WEIGHT MASK

		$n = 3$	$n = 4$	$n = 5$
Dynamic	$a = 0.3$	43.86	43.85	43.84
	$a = 0.4$	43.86	43.86	43.85
	$a = 0.5$	43.85	43.85	43.86
Constant	$a = 1.0$	43.80		

It's evident that the performance of our method is further enhanced with the use of the proposed dynamic weight masks, compared to the PSNR of 40.80dB with a constant mask. Furthermore, from Table III, it can be observed that the dynamic mask is quite robust to the parameters a and n .

B. Comparison Methods

We compare our proposed method with various types of MAR methods, including classical algorithms and deep learning algorithms, unsupervised methods and supervised methods.

The classical methods include **LI** [3] and **NMAR** [4] which involve inpainting the metal-affected regions in the sinogram domain.

Unsupervised deep-learning methods include **CycleGAN** [16], **ADN** [14], and **Score-MAR** [19]. Among these, CycleGAN and ADN are methods that utilize unpaired clean images and metal artifact images to learn style transfer in the image domain. Although CycleGAN is not specifically designed for MAR, it can be applied to metal artifact reduction. ADN is tailored for MAR and consequently exhibits superior performance. Score-MAR employs a pre-trained score model as a prior for MAR. Its solution primarily involves fusing the score prior with known likelihood in the sinogram domain. This is similar to the sinogram inpainting module in our method, while the main difference lies in its operation not being conducted on the predicted initial image. Furthermore, the original Score-MAR work mainly focuses on introducing a generalized framework for solving inverse

problems, hence its experimental conditions for MAR aren't stringent, such as utilizing only parallel beam projections. In the implementation of Score-MAR, to ensure fairness, we employ the same pre-trained model as in our approach⁴.

Additionally, we also compare two supervised learning methods. The first is **CNNMAR** [10], an earlier approach that utilizes a convolutional neural network to predict a prior image for sinogram inpainting. The second is **Indudonet+** [9], which unfolds the reconstruction process to achieve dual-domain learning. It currently holds the state-of-the-art performance on the synthetic dataset.

C. Comparison on Synthetic Data

We first conduct the comparison methods and our method on the synthetic DeepLesion dataset. The metrics of the MAR results are shown in Table IV. Based on the size of the metal implants, the test data is divided into five groups to calculate average metrics for each group. Finally, the overall average metrics are also calculated. From Table IV, it can be observed that our method achieves the best overall average performance among unsupervised algorithms, and surpassing the earlier supervised method CNNMAR, but still with a certain gap compared to the state-of-the-art supervised method InDuDoNet+. Among the unsupervised methods, CycleGAN and ADN, which operate solely in the image domain, perform poorly on large metallic implants but perform better on smaller ones. Our method, benefiting from dual-domain information, performs better on large metal artifacts. Score-MAR's limited performance is attributed to its use of score priors only for sinogram inpainting. This highlights the advantages of using the diffusion priors in dual domains.

Fig. 6 displays the visual effects of different methods' MAR results. As Fig. 6 shows, metal implants can introduce severe streak artifacts in CT images. While LI and NMAR significantly mitigate metal artifacts by performing inpainting in the sinogram domain, they introduce new artifacts due to the discontinuity between inpainted and known parts of the sinogram. CNNMAR improves upon NMAR using convolutional neural networks, but its results still exhibit some artifacts like NMAR. InDuDoNet+ achieves excellent results by supervised learning in dual domains, yet residual streak

⁴In theory, score models and diffusion models are equivalent.

TABLE IV

PSNR/SSIM OF DIFFERENT MAR METHODS ON SYNTHETIC DEEPLesion DATASET, WHERE BOLD REPRESENTS THE BEST RESULT AMONG UNSUPERVISED METHODS, AND AN ASTERISK (*) REPRESENTS THE BEST RESULT INCLUDING SUPERVISED METHODS.

	Methods	Large metal		→	Small metal		Average
	MA	28.99/0.635	30.03/0.766	33.05/0.803	36.33/0.832	37.38/0.853	33.89/0.798
Classical	LI [3]	37.31/0.894	37.62/0.915	39.15/0.929	41.84/0.943	42.36/0.948	40.11/0.931
	NMAR [4]	38.16/0.909	38.30/0.924	39.92/0.934	41.80/0.938	43.74/0.950	40.55/0.934
Supervised	CNNMAR [10]	39.29/0.916	39.61/0.933	41.43/0.945	42.92/0.951	43.13/0.953	41.64/0.943
	InDuDoNet+ [9]	44.17*/0.991*	45.52*/0.994*	48.63*/0.995*	53.87*/0.998*	54.63*/0.998*	50.33*/0.996*
Unsupervised	CycleGAN [16]	36.04/0.957	38.62/0.974	41.00/0.977	43.44/0.983	44.19/0.985	41.40/0.978
	ADN [14]	36.43/0.966	41.76/0.984	42.22/0.985	45.38/0.989	46.13/0.990	43.28/0.985
	Score-MAR [19]	41.73/0.985	41.35/0.985	41.35/0.985	42.58/0.987	44.21/0.990	43.04/0.988
	DuDoDp (Ours)	42.81/0.986	42.43/0.986	43.42/0.988	44.78/0.990	44.89/0.991	43.86/0.989

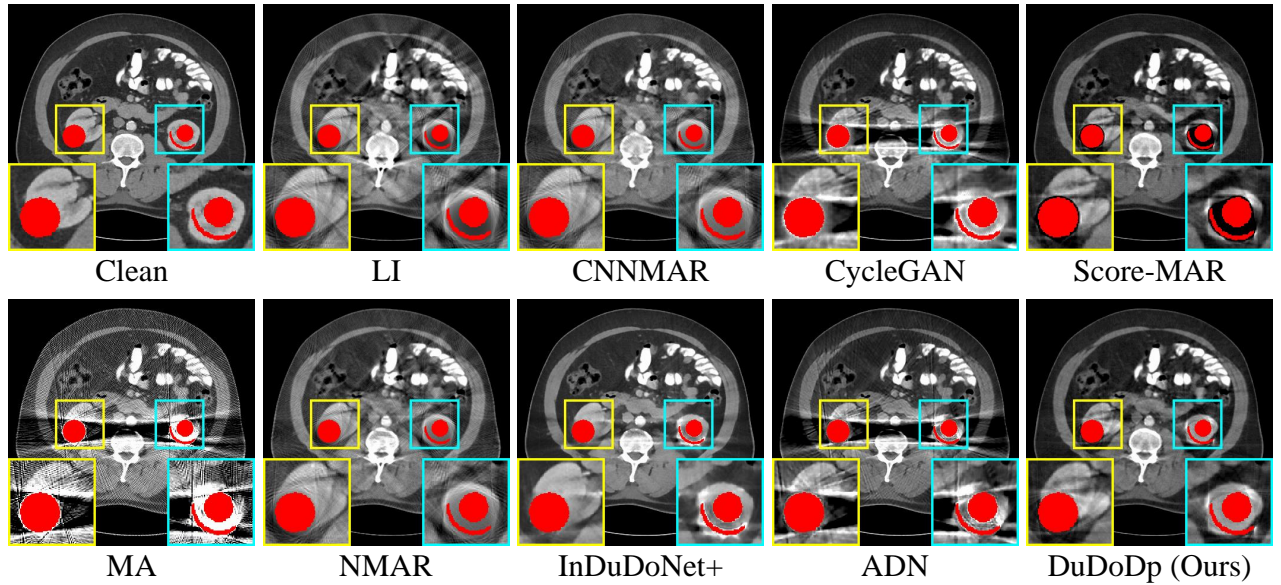
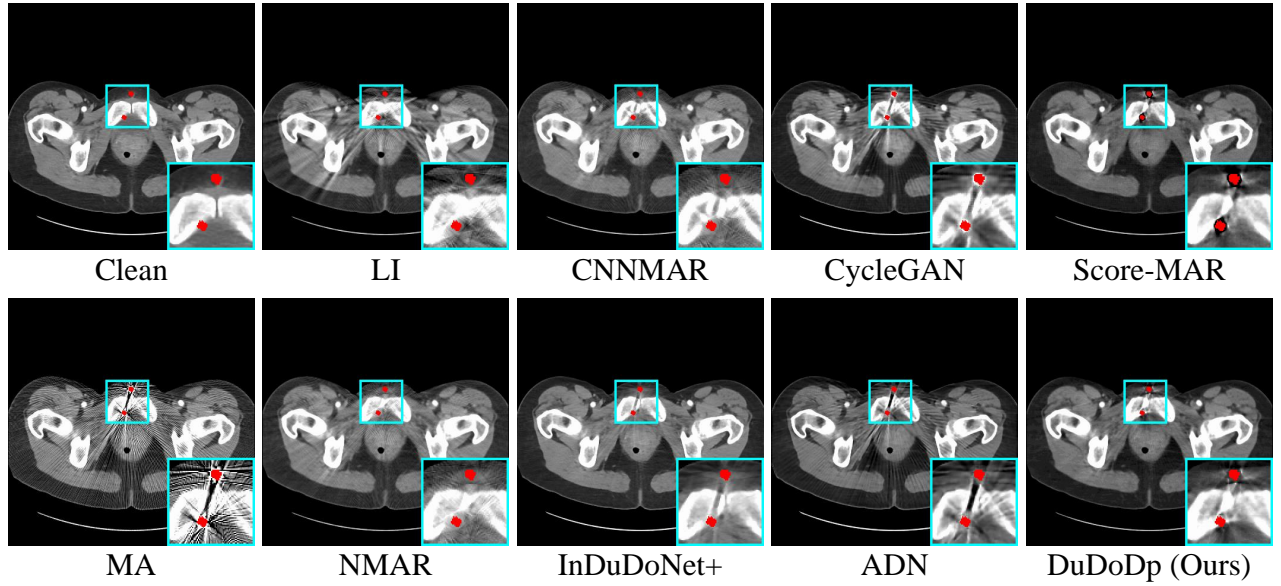


Fig. 6. Visual results of different MAR methods on synthetic DeepLesion dataset. The display window is $[-175, 275]$ HU.

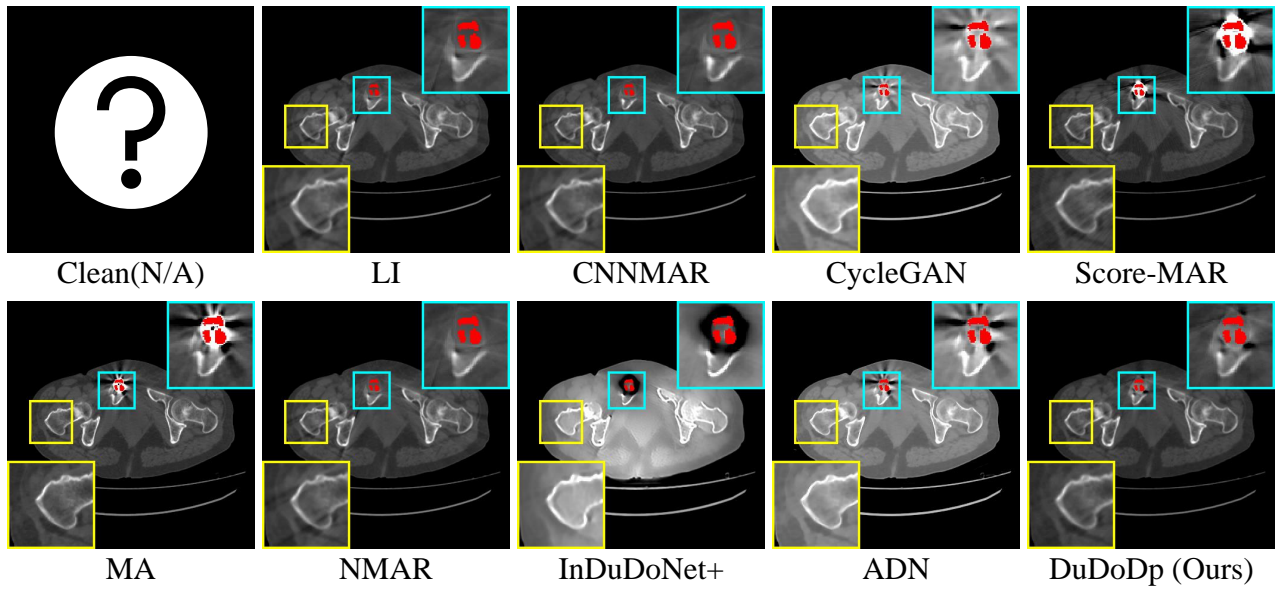


Fig. 7. Visual results of different MAR methods on clinical CTPelvis dataset. The display window is $[-500, 500]$ HU.

artifacts are visible in its output image, especially as shown in Fig. 6(b).

CycleGAN and ADN employ unsupervised learning in the image domain to map metal artifact images to clean images. However, due to the complexity and severity of metal artifacts, as seen in Fig. 6, they struggle to effectively remove streak artifacts, especially with larger metal implants.

Both Score-MAR and our method utilize deep generative models as priors. Their results appear more realistic visually than other methods. However, Score-MAR solely uses the score priors for sinogram inpainting, which leads to substantial errors around metal implants. In contrast, our method, through iterative dual-domain processing, restores a natural and realistic appearance around the metal implants.

D. Comparison on clinical Data

Fig. 7 shows the results of different methods on the clinical dataset. The images depict a pelvic CT slice. Due to the presence of metallic implants, significant artifacts are observed around the metal regions. However, the impact on areas farther from the metallic implants is relatively minor. Visually, traditional methods LI and NMAR have achieved promising outcomes, as indicated by the light blue region of interest (ROI), where they manage to achieve good restoration around the metal areas. Similarly, CNN-enhanced NMAR, or CNNMAR, also exhibits a similar effect. However, these three methods introduce new artifacts in regions away from the metallic implants, as demonstrated by the yellow ROI.

Purely image-based unsupervised methods, including CycleGAN and ADN, exhibit significant deviations in the overall grayscale prediction. This discrepancy could arise from the learned image domain translation not aligning well with the clinical data due to domain gaps. Moreover, these methods are unable to fully leverage the information present in the sinogram. While they don't introduce new artifacts in the

yellow ROI region, they also fail to remove the artifacts near the metal implants.

Surprisingly, InDuDoNet+ fails entirely on the clinical dataset. This could be attributed to its complex architecture overfitting to the simulated data, making it unsuitable for generalization to different datasets.

Score-MAR partially mitigates the metal artifacts, yet there remains an unnatural region around the metallic implant. In comparison to the aforementioned methods, our approach not only successfully reduces the artifacts around the metal but also refrains from introducing new artifacts in other regions. Considering these aspects, our method exhibits the most favorable visual results among all comparison methods, highlighting its potential applicability in clinical settings.

V. DISCUSSION AND CONCLUSION

A. Discussion

A potential way for further enhancing our algorithm's performance lies in adopting distinct image fusion strategies for varying sizes of metallic implants. As evident from Table IV, in experiments involving small metallic implants, our algorithm's metrics are inferior to those of ADN, a pure image-domain algorithm. This observation suggests that when dealing with smaller metallic implants, the metal artifact images still contain substantial clean image information. Consequently, an increased addition of metal artifact images during the image fusion stage could potentially lead to a further improvement in algorithm performance.

We introduce dynamic weight masks to incorporate the diffusion priors in the image domain. The dynamic masks are designed to rectify the newly introduced artifacts after inpainted sinogram reconstruction and they correlate with the timestep t . Despite the enhancement offered by the dynamic masks, its scope remains somewhat limited. Therefore, We consider that these weight masks can also be content-dependent, resulting in different masks for different images.

Such an approach would enhance the adaptability of our algorithm and is an aspect worth investigating.

Prompted by the above two points, the question arises: how can we derive the most suitable weight masks based on image content, shape of the metallic implant, and timestep t ? Manual design of a function is inherently suboptimal in this context. Therefore, we propose the idea of utilizing paired data to learn the image fusion, transforming our method into a model-based supervised learning approach. Although this deviates somewhat from our original motivation, it's foreseeable that such an approach could significantly enhance the performance of our algorithm. This might position our method to be comparable with state-of-the-art supervised learning algorithms like InDuDoNet+. It remains an avenue to be explored in the future.

B. Conclusion

In this paper, we propose DuDoDp for metal artifact reduction, a dual domain method with diffusion priors. Firstly, we train a denoising diffusion probabilistic model with clean CT images. To introduce the diffusion priors to the solving of MAR, we formulate an optimization problem at each timestep of the diffusion model, which solution corresponds to a sinogram inpainting module. After, we propose to fuse the reconstructed image of the inpainted sinogram, the diffusion prior image, and the metal artifact image to make better use of the image domain information. To better control the weights of image fusion, we design dynamic weight masks to further enhance performance. The ablation studies show that the modules proposed in our approach positively contribute to the results of MAR. The results on both the synthetic and clinical datasets have demonstrated that our method outperforms all other unsupervised methods and surpasses earlier supervised MAR method. We believe that our work holds significant implications in exploring the application of deep generative models in the field of MAR. This could potentially extend the use of metal artifact reduction techniques to scenarios where paired training data is scarce.

ACKNOWLEDGMENT

We express our gratitude to the codes of PatchDiffusion-Pytorch [25] and guided-diffusion [26] that facilitate the pre-training of our diffusion model.

REFERENCES

- [1] B. De Man, J. Nuyts, P. Dupont, G. Marchal, and P. Suetens, "Metal streak artifacts in x-ray computed tomography: a simulation study," in *1998 IEEE Nuclear Science Symposium Conference Record. 1998 IEEE Nuclear Science Symposium and Medical Imaging Conference (Cat. No. 98CH36255)*, vol. 3. IEEE, 1998, pp. 1860–1865.
- [2] H. S. Park, S. M. Lee, H. P. Kim, J. K. Seo, and Y. E. Chung, "Ct sinogram-consistency learning for metal-induced beam hardening correction," *Medical physics*, vol. 45, no. 12, pp. 5376–5384, 2018.
- [3] W. A. Kalender, R. Hebel, and J. Ebersberger, "Reduction of ct artifacts caused by metallic implants," *Radiology*, vol. 164, no. 2, pp. 576–577, 1987.
- [4] E. Meyer, R. Raupach, M. Lell, B. Schmidt, and M. Kachelrieß, "Normalized metal artifact reduction (nmr) in computed tomography," *Medical physics*, vol. 37, no. 10, pp. 5482–5493, 2010.
- [5] W.-A. Lin, H. Liao, C. Peng, X. Sun, J. Zhang, J. Luo, R. Chellappa, and S. K. Zhou, "Dudonet: Dual domain network for ct metal artifact reduction," in *Proceedings of the IEEE/CVF Conference on Computer Vision and Pattern Recognition*, 2019, pp. 10512–10521.
- [6] H. Wang, Y. Li, H. Zhang, J. Chen, K. Ma, D. Meng, and Y. Zheng, "Indudonet: An interpretable dual domain network for ct metal artifact reduction," in *Medical Image Computing and Computer Assisted Intervention–MICCAI 2021: 24th International Conference, Strasbourg, France, September 27–October 1, 2021, Proceedings, Part VI* 24. Springer, 2021, pp. 107–118.
- [7] H. Wang, Y. Li, D. Meng, and Y. Zheng, "Adaptive convolutional dictionary network for ct metal artifact reduction," in *The 31st International Joint Conference on Artificial Intelligence*. IEEE, 2022.
- [8] B. Zhou, X. Chen, S. K. Zhou, J. S. Duncan, and C. Liu, "Dudodr-net: Dual-domain data consistent recurrent network for simultaneous sparse view and metal artifact reduction in computed tomography," *Medical Image Analysis*, vol. 75, p. 102289, 2022.
- [9] H. Wang, Y. Li, H. Zhang, D. Meng, and Y. Zheng, "Indudonet+: A deep unfolding dual domain network for metal artifact reduction in ct images," *Medical Image Analysis*, vol. 85, p. 102729, 2023.
- [10] Y. Zhang and H. Yu, "Convolutional neural network based metal artifact reduction in x-ray computed tomography," *IEEE transactions on medical imaging*, vol. 37, no. 6, pp. 1370–1381, 2018.
- [11] X. Huang, J. Wang, F. Tang, T. Zhong, and Y. Zhang, "Metal artifact reduction on cervical ct images by deep residual learning," *Biomedical engineering online*, vol. 17, pp. 1–15, 2018.
- [12] I. Goodfellow, J. Pouget-Abadie, M. Mirza, B. Xu, D. Warde-Farley, S. Ozair, A. Courville, and Y. Bengio, "Generative adversarial networks," *Communications of the ACM*, vol. 63, no. 11, pp. 139–144, 2020.
- [13] J. Wang, Y. Zhao, J. H. Noble, and B. M. Dawant, "Conditional generative adversarial networks for metal artifact reduction in ct images of the ear," in *Medical Image Computing and Computer Assisted Intervention–MICCAI 2018: 21st International Conference, Granada, Spain, September 16–20, 2018, Proceedings, Part I*. Springer, 2018, pp. 3–11.
- [14] H. Liao, W.-A. Lin, S. K. Zhou, and J. Luo, "Adn: artifact disentanglement network for unsupervised metal artifact reduction," *IEEE Transactions on Medical Imaging*, vol. 39, no. 3, pp. 634–643, 2019.
- [15] M. Du, K. Liang, L. Zhang, H. Gao, Y. Liu, and Y. Xing, "Deep-learning-based metal artefact reduction with unsupervised domain adaptation regularization for practical ct images," *IEEE Transactions on Medical Imaging*, 2023.
- [16] J.-Y. Zhu, T. Park, P. Isola, and A. A. Efros, "Unpaired image-to-image translation using cycle-consistent adversarial networks," in *Proceedings of the IEEE international conference on computer vision*, 2017, pp. 2223–2232.
- [17] X. Huang, M.-Y. Liu, S. Belongie, and J. Kautz, "Multimodal unsupervised image-to-image translation," in *Proceedings of the European conference on computer vision (ECCV)*, 2018, pp. 172–189.
- [18] Y. Song, J. Sohl-Dickstein, D. P. Kingma, A. Kumar, S. Ermon, and B. Poole, "Score-based generative modeling through stochastic differential equations," in *International Conference on Learning Representations*, 2021. [Online]. Available: <https://openreview.net/forum?id=PxTIG12RRHS>
- [19] Y. Song, L. Shen, L. Xing, and S. Ermon, "Solving inverse problems in medical imaging with score-based generative models," in *International Conference on Learning Representations*, 2022. [Online]. Available: <https://openreview.net/forum?id=vaRCHVj0uGI>
- [20] J. Ho, A. Jain, and P. Abbeel, "Denoising diffusion probabilistic models," *Advances in Neural Information Processing Systems*, vol. 33, pp. 6840–6851, 2020.
- [21] J. Song, C. Meng, and S. Ermon, "Denoising diffusion implicit models," *arXiv preprint arXiv:2010.02502*, 2020.
- [22] K. Yan, X. Wang, L. Lu, L. Zhang, A. P. Harrison, M. Bagheri, and R. M. Summers, "Deep lesion graphs in the wild: relationship learning and organization of significant radiology image findings in a diverse large-scale lesion database," in *Proceedings of the IEEE Conference on Computer Vision and Pattern Recognition*, 2018, pp. 9261–9270.
- [23] L. Yu, Z. Zhang, X. Li, and L. Xing, "Deep sinogram completion with image prior for metal artifact reduction in ct images," *IEEE transactions on medical imaging*, vol. 40, no. 1, pp. 228–238, 2020.
- [24] P. Liu, H. Han, Y. Du, H. Zhu, Y. Li, F. Gu, H. Xiao, J. Li, C. Zhao, L. Xiao *et al.*, "Deep learning to segment pelvic bones: large-scale ct datasets and baseline models," *International Journal of Computer Assisted Radiology and Surgery*, vol. 16, pp. 749–756, 2021.
- [25] T. Luhman and E. Luhman, "Improving diffusion model efficiency through patching," *arXiv preprint arXiv:2207.04316*, 2022.
- [26] P. Dhariwal and A. Nichol, "Diffusion models beat gans on image synthesis," *Advances in neural information processing systems*, vol. 34, pp. 8780–8794, 2021.